Title: Low-energy scanning transmission electron microscopy applied to ice-embedded biological macromolecules

Running title: (same as above)

Authors: Hidehito Adaniya*, Martin Cheung, Masao Yamashita, Seita Taba, Cathal Cassidy, Tsumoru Shintake

Address: Okinawa Institute of Science and Technology Graduate University, 1919-Tancha, Onna-son Okinawa, 904-0495 Japan,

Phone: +81-(0)98-966-1571, **Fax:** +81-(0)98-966-1064

***Corresponding author: Hidehito Adaniya** hidehito.adaniya@oist.jp

Others email list: Martin Cheung mpcheung18@gmail.com, Masao Yamashita masao.yamashita@oist.jp, SeitaTaba seita.taba@oist.jp, Cathal Cassidy c.cassidy@oist.jp, Tsumoru Shintake shintake@oist.jp

Keywords: low-energy, STEM imaging, cryo-EM, biological macromolecule, image contrast, electron scattering

Total number of pages: 25

Total number of figures: 7

Low-energy scanning transmission electron microscopy applied to ice-embedded biological macromolecules

Hidehito Adaniya*, Martin Cheung, Masao Yamashita, Seita Taba, Cathal Cassidy, Tsumoru Shintake

Okinawa Institute of Science and Technology Graduate University, 1919-Tancha, Onna-son Okinawa, 904-0495 Japan,

Keywords: low-energy, STEM imaging, cryo-EM, biological macromolecule, image contrast, electron scattering

Abstract

In this report, we applied annular bright-field (ABF) and annular dark-field (ADF) low-energy (30 keV) scanning transmission electron microscopy (STEM) imaging to a vitreous ice-embedded biological macromolecule, T4 phage, to investigate the applicability of these methods for morphological investigation and sample screening. Multiple camera lengths were examined to find the optimal acceptance angle for both modes. Image clarity differed substantially between the modes, with the presence of ice also strongly influencing the quality of acquired micrographs. In ADF mode, the proper discrimination of electrons scattered by the specimen from those scattered by the background ice was found to be difficult owing to the severe overlap of the scattered electrons. The resulting micrographs lacked clarity, and the ice-embedded phage particles could only be discerned after post-processing image adjustment. However, in ABF mode, despite similar overlapping of the scattered electrons, it was possible to assess the morphology and intactness of the specimen in the embedding ice, suggesting that this mode may find utility in low-energy cryo-STEM imaging methods.

Introduction

Low-energy scanning transmission electron microscopy (STEM) has been widely used in the study of soft materials and biological specimens because of the enhanced image contrast, reduced knock-on damage, and analytical sensitivity of this approach. The potential for non-destructive imaging of damage-prone samples with low-energy STEM has also been demonstrated [Ultramicroscopy vol.145][Bayer et al][Ogawa et al][Ilett et al], and with a cold-field emission (CFE) gun and aberration correction, image resolution with this method is now approaching the atomic scale. Low-energy STEM thus increases the resolving power of conventional scanning electron microscopy (SEM)-based microscopes.

Image formation in the two major STEM imaging modes, namely bright-field and dark-field, depends on the detection angles of the scattered electrons. In both modes, elastically and inelastically scattered electrons can be used to generate images, with the preservation of the coherence of the scattered electrons not being essential in general. Furthermore, contrast inversion and the loss of certain frequencies, which occurs in interference imaging methods such as transmission electron microscopy (TEM), become irrelevant. The measured signal intensities can therefore be directly associated with the properties of the sample, such as the density, thickness, and constituent elements, and could be beneficial to samples with substantial inelastic scattering. These characteristics of STEM have been found to be especially valuable in high-energy tomographic imaging of relatively thick, high-mass-density biological samples, which can be difficult to image by conventional coherent TEM [Tanaka] [Wolf et al] [Kirchenbuechler et al].

A limited number of studies have applied STEM to thin, low-mass-density ice-embedded biological macromolecules, such as viral specimens [Elad et al], because of the weak scattering power of such samples and thus poor intensities of scattered electrons. Instead, such specimens have been largely restricted to conventional TEM imaging, which has the advantage of being able to utilize the interference of phase shifts in the electron wave to generate image contrast from weak-scattering samples. However, with conventional TEM, successful imaging requires that inelastically scattered electrons are minimized in order to retain coherence of the scattered electrons. This is also true for low-energy cryo-TEM and cryo-holography, which involve substantially greater phase shifts and scattering cross-sections [Majorovits et al][Cheung et al 1].

To the best of our knowledge, the only studies published thus far on cryo-imaging with low-energy STEM have been by researchers at Nagoya University and Hitachi High-Technologies, Japan who, in a pioneering study, developed a special cryo-transfer holder and anti-contamination trap system that can enclose the tip of the holder and can accommodate slush nitrogen in its double-pipe structure to readily control the temperature of the holder tip to between −100°C and −190°C. These advances allow for efficient sublimation/absorption of ice water molecules in the vacuum environment of the microscope (~5×10^{-6} Pa), which minimizes frost contamination as well as the degradation of the ice-embedded specimen, thereby retaining high transmission of the incident electrons. Using a CFE gun-equipped SEM (Hitachi SU9000) operating in BF mode, they successfully visualized the organelles, such as mitochondria, endoplasmic reticulum, and ribosomes, of ice-embedded eukaryotic cells and tobacco mosaic virus [Usukura et al]. In the present study, we also sought to assess the potential of low-energy cryo-EM by applying 30 keV STEM imaging to ice-embedded T4 phage, with particular focus on the effect of detection angles in ABF and ADF modes on their capacity to visualize the morphological features of the sample and on the ice embedding/sample preparation conditions for successful imaging in this low-energy regime.

Materials and Methods

1: Low-energy cryo-STEM

At 30 keV, the elastic and inelastic scattering cross-sections of biological macromolecules are expected to be larger than those with conventional cryo-imaging at 100–300 keV, which results in enhanced image contrast. For example, the scattering cross-sections of carbon-based materials are approximately two-and-a-half to three times greater at 30 keV than at 100 keV [Henderson], thus implying a reduction in the elastic and inelastic mean free paths (MFP and IMFP, respectively) of approximately one-third at 30 keV. While the precise MFP and IMFP values for carbon at 30 keV have yet to be determined, a reduction of this magnitude would give values of 50–60 nm and 15–18 nm, respectively [Reimer][Angert et al]. Similar reductions of the MFP and IMFP are likely to occur for carbon-based macromolecules. In the case of our test specimen T4 phage, the IMFP becomes five times smaller than the thickness of the head (~90 nm) at 30 keV, which leads to i) an increase in total electron scattering from the specimen as a consequence of a vast increase in inelastic scattering and multiple scattering events and ii) an increase in angular distributions, which would extend beyond that of a singly scattered electron by a factor of approximately two to five [Egerton], yielding a substantial outer fraction in the angular distribution that is directly associated with the amplitude of the signal from the specimen in the STEM image.

While the MFP and IMFP of vitreous ice at 30 keV have also not yet been determined, similar reductions from values at100 keV would give an IMFP of 30–60 nm [Angert et al][Shinotsuka et al] and MFP of 30–70 nm [Feja et al][Angert et al]. These values are smaller than the predicated thickness of the vitreous ice (approximately 80–100 nm) surrounding embedded phage particles when prepared using the perpetually-hydrated graphene oxide (GO) method [Cheung et al 2][Cho et al] and would thus likely result in increases in the scattering cross-sections and angular spreads. An increase in inelastically scattered electrons has been shown to be problematic in low-energy TEM and holography [Majorovits et al][Cheung et al 1] but would not be of much concern in STEM imaging.

However, an excessive angular spread of the scattering distribution from the background ice would obscure the image, and imaging in STEM is therefore contingent on the careful selection of the optimal acceptance angle (i.e., camera length).

2: Low-energy STEM microscope

This work was conducted on the Diffraction Microscope with Focused ion beam (DMF4000) at the Okinawa Institute of Science and Technology Graduate University, originally developed for low-energy cryo-holographic and diffraction imaging. A detailed account of the microscope's hardware was presented in our previous study [Adaniya et al]. In short, the microscope is equipped with a custom STEM detector comprising a P47 scintillator-covered detector (16 mm in diameter) with a small hole (1.4 mm in diameter) in the center, which functions as the annular bright-field (ABF) and annular dark-field (ADF) detector by adjusting the microscope optics (Fig. 1). Downstream of the sample stage, a set of alignment coils and a projector lens are employed to direct the scattered electrons towards the STEM detector. Owing to the limited room available at the projector lens, the maximum cut-off angle for ADF was limited to ~100 mrad in this work. ABF and ADF images were obtained sequentially by adjusting the optics settings. For details on the operation of DMF4000 in STEM and holographic imaging modes, please refer to previous study [Cheung et al 1].

3: Sample preparation

T4 phage was employed in this study because of its relatively large mass (for single particle cryo-EM studies) and characteristic morphological features, which make it easily recognizable and therefore an appropriate first test sample. Quantifoil grids with holes 2 µm in diameter (R2/2) were used with perpetually-hydrated GO flakes in order to embed T4 phage particles within thin vitreous ice films. Please refer to our previous study for a detailed description of the preparation scheme [Cheung et al 2].

4: Experimental method

Because the constituent elements of ice, O and H, are also major constituent elements of T4 phage (C, N, O, and H), the mass-densities of protein (1.3 g/cm^3), DNA (1.6 g/cm^3), and ice (1.0 g/cm^3) [Reichelt et al] are similar. As a result, the angular distributions of the scattered electrons from the specimen and background ice are also similar. Therefore, careful discrimination of the background electrons is necessary to generate maximum image contrast. To achieve this, we employed multiple camera lengths to find the acceptance angle which gave optimal discrimination of scattered electrons from the specimen from those of the background ice.

Five different camera lengths **(Table 1)** for ABF mode and four for ADF mode (**Table 2**) were used to measure the intensities of relevant electrons scattered by the large polyhedron head (icosahedron) of the phage to evaluate image contrast. We employed an in-focus beam at 30 keV with a 3.7 mrad half-angle impinging beam and 500 nm depth-of-focus. To quantify the visibility of the ice-embedded phage particles, we evaluated the contrast $\Delta I/I_{background}$ (where $\Delta I = |I_{back} - I_{T4}|$, I_{back} is the mean of the background intensity, and I_{T4} is the mean of the T4 phage intensity), which is a direct comparison of the difference in intensities of the scattered electrons from the phage and background (ΔI, the relative luminance of the phage) to that of the background (the background luminance), and the contrast-to-noise ratio (CNR) of ABF, $\Delta I/\sigma_{back}$ (where σ_{back} is the standard deviations of I_{back}), which compares the former to the noise of the latter (square-root of the fluctuation of the background luminance) [Welvaert et al]. CNR is widely employed in medical imaging as a metric for the detectability of clinical lesions with weak activation luminance.

Results

1: Lower magnification ABF imaging with multiple camera lengths

An electron dose of 120 pA was used. Since the same area needed to be scanned sequentially for the five camera lengths, a relatively low magnification of 60,000× [with a field-of-view (FOV) of 5 μm] was employed to mitigate beam damage. Each image comprised 1,000 × 1,000 scan spots with a dwell-time of 30 μs per spot, which provided a 5-nm distance between two successive spots, a total electron dose per spot of 2.3×10^4, and a total electron dose per frame of 2.3×10^{10}. Amplification by the photomultiplier tube (PMT) of the STEM detector was kept constant at the respective camera lengths.

Figures 2(a) to (e) show ABF images of ice-embedded T4 phages and profiles of the intensity and contrast measured across the head of phage A using ABF-1 to -5. Table 3 shows the corresponding CNR values. The measured intensities of the phage heads and backgrounds from the images are plotted in Figure 3(a), and the trends of measured contrast and CNR are shown in Figure 3(b). Interestingly, the intensities of the scattered electrons from the background ice and phage were found to increase monotonically when transitioning from ABF-1 to -5 (Fig. 3 (a)), indicating a substantial angular spread of more than the 3.7 mrad of the impinging beam angle. The similarities in the trends of the intensities could be partially attributed to the presence of the ice layers on and beneath the phages, which could cause the scattering from the combination of phage plus ice to have somewhat similar characteristics to that of just the ice. In the angular range tested, the contrast of the head of the phage remained relatively constant~28% on average for ABF-1 to 5, with a slight reduction for ABF-5, which had the largest outer cut-off angle (OCA). The relatively large errors in the measured contrast were due to the large standard-deviation (SD) in the intensity of the phage head, which can be attributed to its large polyhedron morphology. We observed slight bubbles arising from radiolysis damage of the sample to appear after the fourth single frame scan, even with the 5-nm separation distance between successive scanning spots at the low FOV.

All the camera lengths tested appeared to give equal image contrast of the head of the phage particle assessed in the micrographs. However, as is commonly observed in cryo-EM, areas with thicker embedding ice showed strong suppression of electron scattering, resulting in poor electron transmission and reduced interpretability of the morphologies of the phage particles. We often observed that this effect occurred more severely with smaller OCAs, and it would therefore seem that larger OCAs, such as ABF-4 or -5, would be beneficial because of the larger scattering intensities.

The trend of the CNR was similar to the trend of the scattering intensities, which was largely due to the relatively uniform thickness of background ice (~80–100 nm [Cheung et al 2][Cho et al], as stated in the previous section) and thus similar σ_{back} values at respective camera lengths. Therefore, variances in CNR were largely determined by variances in ΔI, with broad peaks seen for ABF-3 to -5 as a consequence of the larger scattering of electrons. Visually, these CNR values broadly agree with the perceived clarity of the images in Figure 2. For this sample, ABF-4 would appear to be the optimal camera length.

2: Higher magnification ABF imaging

The measurements in the preceding section were repeated with a FOV of 2.5 μm, with a magnification of 120,000×, and ABF-4 to investigate whether more structural information from of T4 phages could be resolved. The electron dose was 150 pA, and the total electrons per scan spot was 2.9×10^4, giving a total dose of 2.9×10^{10} electrons per frame.

An unadjusted ABF-4 image is presented in Figure 4(a) together with an enlarged image of the upper-left area in (b). As can be seen, the distinct morphology of T4 phage is evident with this imaging regime, with the thin filamentous tail and irregularity in mass distribution of the head clearly discernable. The contrast of the head of phage A (in the center of the hole) was measured to be 37 %, which is slightly enhanced compared with the contrast of the head of phage D, possibly because of the thinner embedding ice near the center of the hole. Ice films spanning TEM grid holes are generally thinnest at the center and thickest at the edges (biconcave), which could account for the somewhat weakened contrast of phage D [Cheung et al 2]. The contrast of the heads of phages B and C read below 10% and appeared to have partially lost their head-encapsulated genomic DNA. The contrast of the tails of phages E and F read only ~6%, possibly owing to their small mass-densities and narrow widths, limiting detailed morphological interpretation. The relatively opaque background ice near the heads of these particles could have been caused by the following factors: i) Cheung et al. [Cheung et al 2] showed that for specimens embedded in ice using the perpetually-hydrated GO method, the ice layer conforms with the shape of the specimen. Since T4 phage has a large, irregular shape, we expect the ice to also be irregular in thickness and thicker around the specimens; ii) in addition to this irregular thickness, it is possible that liberated DNA could have mixed with the ice around the phages, resulting in larger scattering angles than the OCA and thus a decrease in transparency.

Degradation of the T4 phages in our sample could have arisen from osmotic shock and/or freeze-thawing during purification and storage, which can cause liberation of the head-encapsulated DNA to the external environment. The ability to identify these degraded T4 phage particles without DNA serves as a useful means of evaluating the quality of the sample. The ABF scheme described here is capable of discerning the stark difference in contrast between these two subsets of T4 phage particles, allowing for degraded particles to be rapidly differentiated from intact particles. We believe that this imaging scheme has the potential to be a rapid sample screening tool.

Bubbles arising from specimen damage by the impinging beam were not observable during the first single-frame scan, possibly because successive scanning spots at our designated FOV were 2.5 nm apart, which was enough to prevent overlap with the 2-nm focus spot of the beam. We note, however, the bubbles were observable with the second and successive frame scans of the same area (not shown in this report).

3: Lower magnification ADF imaging with multiple camera lengths

As with ABF mode, we first imaged the same area at four camara lengths (Table 2) and a FOV of 5 μm in order to find the optimal acceptance angle. The electron dose was 200 pA, and the total electrons per scan spot was 3.9×10^4, giving a total dose of 3.9×10^{10} electrons per a frame. PMT amplification was kept constant.

ADF images of the ice-embedded phage particles using this setup and the respective intensity line profiles of their heads are shown in Figure 5. Owing to the extremely low image contrast with this mode, the raw images (top row in Fig. 5(a)–(d)) have been adjusted to better display the location of the phages (middle row in Fig. 5(e)–(h)). Plots of image contrast and intensities from the phage head and background are shown in Figure 6.

Unlike with ABF mode, we experienced considerable difficulty in obtaining images with clearly visible phage particles using this mode. The measured intensities from the phage and background ice were very similar in magnitude in this angular range, resulting in poor distinguishability with all camera lengths tested, necessitating post-processing image adjustment to even identify the phages in the ice. The trend of the scattering intensities from the background ice suggested that scattering from the ice broadened the beam angle far beyond the incident angle range of 3.7 mrad. Even after adjusting the images, the visibility of the phages did not show substantial improvement with ADF-1, and visualization of phage particles at the edge of the hole remained difficult. The phages became more discernible with ADF-2, which had an inner cut-off angle (ICA) beyond 10 mrad, yielding contrast larger than ~10%. ADF-4 produced the highest contrast at 25–40%; however, the scattering intensities were prohibitively low at only a few percent of those for ADF-2, and image clarity did not substantially improve (Fig. 5 (d) and Fig. 6). The increase in contrast with ADF-4 did not necessarily improve interpretability of the specimen, because of the low scattering intensities; it should be noted that in order to increase the scattering intensities with ADF-4 to enhance the visibility of the phage particles, a far larger dose would be required, which would invariably result in increased radiation damage to the specimen. It should also be noted that using adjusted images and CNR to quantify the visibility of the phage and identify optimal camera lengths should be interpreted with caution. We will limit our discussion to the effect of contrast on the morphological characterization of the sample as this is directly associated with the intensities of the scattered electrons.

In ADF mode, we found that image clarity was strongly influenced by the surface condition of the ice, such as the presence of contaminants, ice thickness, and the run-time of the experiment. There were large variances in contrast among areas of interest even within the same square of the Quantifoil grid, which made judging the optimal camera length difficult. Furthermore, with the minute differences in intensities between the sample and background, practical imaging with this mode was prohibitively difficult, and without post-processing of the images, merely identifying the positions of the embedded phage particles was difficult. ADF-2, which provided the largest ΔI throughout most of this work, allowed for some degree of sample visualization even without image adjustment and was found to be usable for the rapid identification of the positions of the phage particles and assessment of the ice.

4: Higher magnification ADF imaging

Based on the results detailed in the previous section, higher magnification images with ADF-2 (highest scattering intensities) and ADF-4 (nominal highest contrast) were recorded to ascertain whether more structural information could be discerned from the noisy images. The magnification resulted in a FOV of 2.5 μm (as with ABF), and a dose of 200 pA was employed with constant PMT amplification. Also, as in the previous section, the unadjusted (Fig. 7(a) and (b)) as well as adjusted images (Fig. 7(d) and (e)) are presented to better show the embedded phages. Enlarged images of the upper areas of (d) and (e) are also presented in (f) and (g), respectively. An ABF-4 image of the same area obtained at a FOV of 5 μm is also shown for the purpose of comparison in Figure 7(c)**.**

As shown in the adjusted ADF-2 images in Figure 7(d) and (f), the contrast of the intact heads of phages A and B were measured to be ~8%, whereas a vastly higher contrast of ~27% was measured for the same particles with ADF-4 (Fig. 7 (e) and (g)), showing that differences in mass-density strongly manifested as prominent increases in contrast with ADF-4; however, as mentioned in the previous section, this did not result in improved interpretability of the specimen. For degraded phage C in Figure 7 (c) and (d), the apparently empty head and ambient ice showed similar mass-densities and, as a consequence, nearly indistinguishable electron scattering distributions, making the particle difficult to locate and distinguish from the ice. Interestingly, however, the identical phages yielded higher contrast values in ABF mode of ~32% for the intact phage and ~6% for the degraded phage, respectively. It should be noted that although the measured contrast with ADF-4 for the intact phages A and B (~28%) were in a similar range to those measured with ABF-4 (~32%), the visibility of the phage morphologies appeared vastly lower with ADF-4. Image clarity is better reflected by differences in magnitude of ΔI, which directly correlate with differences in scattering intensities at respective angles and was substantially larger with ABF-4. It should also be noted that nominal value of the 'relative contrast' $\Delta I/I_{background}$ undervalues contrast values in ABF images because the background intensity is larger than the signal from the phage, I_{T4}, which is opposite to the situation for ADF images. Bubbles in the ADF images arising from beam damage to the phage particles were also not discernable at this magnification because of the poor resolution of the images in addition to the reasons stated for ABF mode.

As mentioned previously, the ability to identify and distinguish degraded particles is an important factor in assessing the quality of a purified sample. In the ADF-2 and -4 schemes shown here, the differences in mean intensities between the scattered electrons from the degraded and intact phage particles and those from the background ice were minor, making it difficult to clearly differentiate between these subsets of particles without adjustment of the images. Furthermore, even with adjustment, the poor contrast of the degraded particles against the surrounding ice made visualization of these particles difficult; this was particularly evident for degraded particles located near the edges of the grid holes, where ice is generally thicker (e.g., phage C in Fig. 7(a) and (b)). Therefore, for the rapid assessment of sample quality and 'intactness', ADF performs worse than ABF for the sample tested here.

Discussion

1: On image contrast

ABF imaging shows promise as a tool for the visualization of ice-embedded bio-specimens, with the overall morphology and structural features of our T4 phage sample clearly resolvable in micrographs. ABF images are formed by the integration of electrons scattered at low angles over a width of only a few milliradians (including the impinging angle), and the dark appearance of the specimen is made by the 'depletion' of electrons due to scattering by the specimen; it is essentially the difference in the intensities of the scattered electrons from the background ice and the specimen within the integration width and thus depends on differences in their respective thicknesses and mass-densities, which manifest practically as their MFPs and IMFPs.

Since the sample preparation method used in this study was expected to create frozen grids with phage particles embedded within vitreous ice films not much thicker than the phage head [Cheung et al 1], the angular distribution of the scattered electrons from the phage particles were far wider than those from the background ice because of the shorter MFP and IMFP of the phages than the vitreous ice, as mentioned in Section II. This results in a substantial depletion of electrons in the low angular range. The strong contrast generated by the heads of the phages in ABF mode (Fig. 2 and Fig. 4) supports this scattering mechanism. This contrast generation mechanism also explains why the filamentous phage tails and degraded phage particles, which have mass-densities closer to that of the ambient ice, showed weaker contrast. We also observed, however, an angular spread of electrons scattered by the background ice, albeit at smaller angles than that phage particles.

ADF imaging has been mostly used for amplitude contrast imaging, such as Z-contrast, in which the sample has significantly stronger scattering at high scattering angles than the background substrate. In this imaging modality, specimen contrast (bright signal in the micrograph) is predominantly generated by the intensity of scattered electrons from the specimen. However, the situation for ice-embedded specimens is vastly different. As briefly discussed in Section II, since the MFP and IMFP of 30 keV electrons in ice is comparable, or even shorter, than the typical thickness of the ~100 nm vitreous ice films in macromolecular cryo-EM [Cho et al] [Cheung et al 2], the impinging electrons are scattered over a wide angular range and far beyond the impinging cone shown in Figures 5 and 6.

A previous electron scattering experiment conducted at 120 keV showed that the angles of electrons scattered by a 100-nm thick ice film were distributed over a wide angular range, with approximately 20% of the scattered electrons estimated to be distributed beyond ~4 mrad (our approximate impinging angle) and forming a substantial 'outer-fraction' in the angular distribution [Angert et al]. At 30 keV, this outer-fraction is expected to increase by a factor of approximately three because of the vast increase in multiple scattering events [Egerton], which interfere, or ‘overlap’, with the scattered electrons from the specimen. This overlap becomes worse as the mass-density of the specimen approaches that of the vitreous ice, which was shown here by the poor contrast of the phage tails and degraded phage particles. In this regard, the embedding ice should be as thin as possible while still fully encapsulating the sample. Interestingly, the majority of scattered electrons from the phages and background ice appear to have been distributed below 30 mrad, as shown for ADF-4 in Figures 5 and 6. Macromolecular specimens of higher mass-density or those containing heavier elements that scatter electrons beyond this angle would be interesting targets for further studies.

2: On the imitations of this work

In the micrographs recorded by the two imaging schemes presented here, the internal structures of the phages were not resolvable, which we attribute to the low energy of the irradiating beam. The MFP and IMFP of electrons at 30 keV are far shorter than the size of the phage head, suggesting that the majority of impinging electrons would have undergone multiple scattering events when passing through the head, thus resulting in a diffused focus spot and partial backscattering. Another cause may have been the lack of the brightness of the beam; the electron beam employed in DMF4000 is generated by a Schottky emitter that creates an estimated focus spot of ~2 nm in diameter [Adaniya et al], which necessitates the use of a FOV no smaller than 2.5 μm in order to allow a separation between successive scan spots of 2.5 nm. We were not able to capture images at a magnification higher than 120,000×, which would lead to a FOV smaller than 2.5 μm, since obvious beam damage was observed beyond the first single frame scan. The limited brightness of the beam at the required FOV may also have hampered visualization of more detailed morphological features.

Long tail fibers on the distal end of the phage tail were also not visible in micrographs produced in this study as each tail fiber, approximately 3–4 nm in width, was only scanned twice at this scan spot size and magnification. SEM/STEM equipped with CFE guns with focus spots a few angstroms in diameter are already widely available, although the application of these microscopes to ice-embedded macromolecules is particularly challenging. These microscopes use electron beams with limited energy, and such beams would be diffused by the embedding ice. Electron scattering from fine structures much thinner than the thickness of the embedding ice film, such as the long tail fibers, would likely be overwhelmed by scattering from the ice and difficult to discern with our current detector. The sensitivity and response of the detector as well as the collection efficiency of the scintillated photons would need to be improved in order to visualize weak scatterers. Moreover, increasing magnification results in image blurring due to drift of the cryo-transfer holder and would also become an issue. The scanning speed of our current imaging setup (1,000 × 1,000 pixels at 30 s per frame) would also require improvement to increase image stability. Therefore, for higher resolution cryo-STEM imaging of ice-embedded macromolecules, in addition to preparing thinner embedding ice, the aforementioned factors would need to be considered.

Recently, Lazić and colleagues [Lazić et al] demonstrated the application of integrated Differential Phase Contrast (iDPC)-equipped STEM at 300 keV to ice-embedded tobacco mosaic virus. By applying three-dimensional reconstruction techniques to phase images, the authors achieved a resolution comparable to that of conventional cryo-TEM. The applicability of iDPC detectors to the imaging of ice-embedded bio-specimens at 30 keV is unclear; however, cryo-STEM at 300 keV could resolve the aforementioned limitations in this work. Further investigation of the applicability of cryo-STEM to biological macromolecules under various conditions, such as low vs. conventional energy and amplitude vs. phage imaging, is warranted.

Conclusion

We investigated the applicability of low-energy ABF- and ADF-STEM imaging to ice-embedded T4 phage particles. The presence of the background ice was found to vastly weaken the contrast of the phages in both modes. Despite the weakened contrast, however, ABF imaging was able to discern useful structural information of the phages, such as their morphologies and intactness, as well as assessment of the embedding ice. In ADF mode, image clarity was found to be severely degraded by the strong overlap of electrons scattered by the phages and background ice. With the increase in angular range of the scattered electrons, intensities became prohibitively low and, as the result, the discrimination of scattered electrons for practical cryo-imaging was difficult; post-processing image adjustment was necessary for even the basic identification of the phages in the ice. Although the overall morphological structures of the phages were clearly resolvable in ABF mode, internal structures of the head and the long tail fibers were not. An electron beam with higher energy and brightness would be necessary for more detailed structural investigation.

Acknowledgement

We would like to thank Mr. Hidehiro Yamada, Yoichi Ose, Takahiro Yasuda at Hitachi Hi-Tech, and Dr. Jiro Usukura, Dr. Tomoharu Matsumoto at Nagoya University for supportive advice in technical and operational aspects.

This work is supported by Okinawa Institute of Science and Technology Graduate University.

References

Kaiser U and Stöger-Pollach M (ed) (2014) Low-Voltage Electron Microscopy. Ultramicroscopy.145: 1-104

Beyer Y, Beanland R, and Midgley P.A. (2012) Low voltage STEM imaging of multi-walled carbon nanotubes. Micron. 43: 428-434.

Ogawa T, Won Gang G, Thu Thieu M, Kwon H, Jung Ahn S, Hwan Ha T, and Cho B (2017) Graphene-supporting films and low-voltage STEM in SEM toward imaging nanobio materials without staining: Observation of insulin amyloid fibrils. Micron. 96: 65-71.

Ilett M, Brydson R, Brown A, and Hondow N (2019) Cryo-analytical STEM of frozen, aqueous dispersions of nanoparticles. Micron. 120: 35-42.

Tanaka N (2017) *Electron Nano-Imaging: Basics of Imaging and Diffraction for TEM and STEM*. (Springer)

Wolf S, Houben L, and Elbaum M (2014) Cryo-scanning transmission electron tomography of vitrified cells. Nat Methods. 11: 423–428.

Kirchenbuechler D, Mutsafi Y, Horowitz B, Levin-Zaidman S, Fass D, Wolf S G, and Elbaum M (2015) Cryo-STEM Tomography of Intact Vitrified Fibroblasts. AIMS Biophysics. 2: 259-273.

Elad N, Bellapadrona G, Houben L, Sagi I, and Elbaum M (2017) Detection of isolated protein-bound metal ions by single-particle cryo-STEM. Proceedings of the National Academy of Sciences. 114:11139-11144.

Majorovits E, Angert E, Kaiser U, and Schröder R R (2016) Benefits and Limitations of Low-kV Macromolecular Imaging of Frozen-Hydrated Biological Samples. Biophysical Journal. 110:776-784

Cheung M, Adaniya H, Cassidy C, Yamashita M, and Shintake T (2020) Low-energy in-line electron holographic imaging of vitreous ice-embedded small biomolecules using a modified scanning electron microscope. Ultramicroscopy. 209:112883

Usukura J, Narita A, Matsumoto T, Usukura E, Sunaoshi T, Watanabe S, Tamba Y, Nagakubo Y, Mizuo T, Azuma J, Osumi M, Nimura K, Tamochi R, and Ose Y (2021) A cryo-TSEM with temperature cycling capability allows deep sublimation of ice to uncover fine structures n thick ice cells, Scientific Reports. 11: 21406

Henderson R (1995) The potential and limitations of neutrons, electrons and X-rays for atomic resolution microscopy of unstained biological molecules. Quarterly Reviews of Biophysics. 28(2): 171-193.

Kohl H and Reimer L (2008) Transmission Electron Microscopy: Physics of Image Formation, 5th ed (Springer)

Angert I, Burmester C, Dinges C, Rose H, and Schröder R R (1996) Elastic and inelastic scattering cross-sections of amorphous layers of carbon and vitrified ice. Ultramicroscopy. 63:181-192

Egerton R F (2011) Electron Energy-Loss Spectroscopy in the Electron Microscope, 3rd ed (Springer)

Shinotsuka H, Da B, Tanuma S, Yoshikawa H, Powell C J, and Penn D R (2017) Calculations of electron inelastic mean free paths. XI. Data for liquid water for energies from 50 eV to 30 keV. Surface and Interface Analysis. 49:238-252

FEJA B, and AEBI U (1999) Determination of the inelastic mean free path of electrons in vitrified ice layers for on-line thickness measurements by zero-loss imaging, Journal of Microscopy. 193:15-19

Cheung M, Adaniya H, Cassidy M, Yamashita M, Li K L, Taba S, and Shintake T (2018) Improved sample dispersion in cryo-EM using “perpetually-hydrated” graphene oxide flakes, Journal of Structural Biology. 204:75-79

Cho H J, Hyun J K, Kim J G, Jeong H S, Park H N, You D J, and Jung H S (2013) Measurement of ice thickness on vitreous ice embedded cryo-EM grids: investigation of optimizing condition for visualizing macromolecules. J Anal Sci Technol. 4: 7

Adaniya H, Cheung M, Cassidy C, Yamashita M, and Shintake T (2018) Development of a SEM-based low-energy in-line electron holography microscope for individual particle imaging, Ultramicroscopy. 188:31-40

Reichelt R, and Engel A (1984) Monte Carlo calculations of elastic and inelastic electron scattering in biological and plastic materials. Ultramicroscopy. 13:279-293

Welvaert M, and Rosseel Y (2013) On the definition of signal-to-noise ratio and contrast-to-noise ratio for FMRI data. PLoS One. 8(11):e77089

Lazić I, Wirix M, Leidl M L, de Haas F, Beckers M, Pechnikova E V, Müller-Caspary K, Egoavil R, Bosch E G T, and Sachse C (2021) Single-particle cryo-EM structures from iDPC-STEM at near-atomic resolution. bioRxiv.
doi: https://doi.org/10.1101/2021.10.12.464113

	ABF-1	ABF-2	ABF-3	ABF-4	ABF-5
ICA [mrad]	0.5	0.7	0.9	1.3	1.7
OCA [mrad]	3.1	4.1	5.3	7.2	9.6
Camera length [mm]	1,275	979	759	558	416

Table 1. Inner-cutoff-angle (ICA), outer-cutoff-angle (OCA), and camera lengths used for the ABF measurements. Note that ABF-1 to -5 indicates increasing cutoff angles.

	ADF-1	ADF-2	ADF-3	ADF-4
ICA [mrad]	6.0	9.5	20.0	28.1
OCA [mrad]	34.4	54.4	100.0	100.0
Camera length [mm]	116	74	35	25

Table 2. ICA, OCA, and camera lengths used for the ADF measurements. Note that ADF-1 to -4 indicates increasing cutoff angles. The OCAs for ADF-3 and -4 were limited to 100 mrad because of the limited space in the STEM column.

	ABF-1	ABF-2	ABF-3	ABF-4	ABF-5
CNR	13.4	14.1	19.3	22.9	21.4

Table 3. Contrast-to-noise (CNR, $\Delta I/\sigma_{back}$) evaluated from the intensity plots in Figure 3, where σ_{back} is the standard deviation of I_{back} in Figure 3.

Fig. 1 (Top) The low-energy microscope, DMF-4000, originally developed for diffraction and holographic imaging. (Bottom) Illustration of the beam paths for the annular bright-field (ABF)-and annular dark-field (ADF)-scanning transmission electron microscopy (STEM) modes employed in this work. The propagation of the impinging electrons from the electron gun to the STEM detector is depicted by the blue pattern. For illustrative purposes, the impinging beam angle is depicted as being retained downstream of the sample in order to differentiate it from the rays of the scattered electrons, which are depicted by the dotted arrows.

Fig. 2 (Top row) ABF images of ice-embedded T4 phages. (a) to (e) correspond to images of the same area using ABF-1 to -5. (Bottom row) Profiles of the averaged intensities of the region of interest indicated by the line across the head of the phage particle labeled ‘A’ in image (a) and their respective contrast (lines not shown in (b) to (e) for visibility). The average intensities were evaluated over the 10-pixel-wide lines in the images. Evaluation was performed with Gatan *DigitalMicrograph*. Scale bar, 500 nm.

Fig. 3 (Left) Plots of the measured intensities at the head and background of the phages shown in Figure 2. The horizontal-axis corresponds to the ICA of ABF, and the numbers correspond to ABF-1 to -5. The vertical error bars were estimated from the standard deviations of the intensities over the same regions of interest for the intensity measurements. The polyhedron head of T4 phage caused larger standard deviations in the T4 intensities when compared with the ‘flat’ background. Evaluation was performed with Gatan *DigitalMicrograp*h. The horizontal error bars correspond to the uncertainties in the ICA caused by fluctuations in the electric current in the projector lens. (Right) Plots of the contrast measurements in Figure 2 and CNR in Table 3.

Fig. 4 (Top row, (a)) ABF-4 image of ice-embedded T4 phages at a FOV of 2.5 µm. Scale bar, 500 nm. (Top row, (b)) Enlarged image of the upper-left area of (a) including the T4 particles A to E. Scale bar, 250 nm. (Bottom row) Profiles of the averaged intensities of the region of interest indicated by the lines across phages A to F in (a) and respective contrast (lines not shown in (b) for visibility). Profiles across the heads of the phages are shown in A to D, with E and F showing profiles across the tails. Phages B and C exhibit quasi-transparency and substantially weaker contrast, suggesting partial loss of the contents (DNA) of their heads. The average intensities were evaluated over the 20-pixel-wide lines in the images. Evaluation was performed with Gatan *DigitalMicrograp*h.

Fig. 5 (Top row, (a) to (d)) Unadjusted ADF images of ice-embedded T4 phages. (a) to (d) correspond to ADF-1 to -4. The visibility of (d) is extremely weak owing to the poor scattering intensities. (Middle row, (e) to (h)) Adjusted versions of (a) to (d). Adjustments were performed with *Gatan DigitalMicrogaraph*. (Bottom row) Profiles of the averaged intensities of the region of interest indicated by the line across the head of the phage A and the respective contrast (lines not shown in (f) to (h) for visibility). The average intensities were evaluated over the 10-pixel-wide lines in the images. Evaluation was performed with Gatan *DigitalMicrograp*h. Scale bar, 500 nm.

Fig. 6 Plots of the measured intensities of the head, background, and contrast of phage A in Figure 5. The ICAs on the horizontal-axis correspond to ADF-1 to -4 in Table 2. The vertical error bars were estimated from the standard deviations of the intensities over the same regions of the interest for the intensity measurements. Evaluation was performed with Gatan *DigitalMicrograp*h. The horizontal error bars correspond to the uncertainties in the ICA caused by fluctuations in the electric current in the projector lens.

Fig. 7 (Top row, (a) and (b)) Unadjusted images of ice-embedded T4 phages with ADF-2 and ADF-4, obtained at a FOV of 2.5 µm. The visibility of (b) is extremely weak owing to the poor scattering intensities with ADF-4. (Top row, (c)) unadjusted image of the same area with ABF-4, obtained at a FOV of 5 µm. (Second row, (d) and (e)) Adjusted versions of (a) and (b). Scale bar in (a) to (e), 500 nm. (Second row, (f) and (g)) Enlarged image of the upper area of (d) and (e) including the T4 particles A, B, and C. Scale bar in (f) and (g), 250 nm. (Third to fifth rows) Profiles of the averaged intensities of the regions of interest indicated by the lines across the heads of phages A to C (indicated in (d)) and respective contrast (lines not shown in (c), and (e) to (g) for visibility). Phage C appeared to have partially lost the contents of the head, becoming nearly indistinguishable from the ambient ice with ADF-4. The average intensities were evaluated over the 20-pixel-wide lines in the ADF image and 10-pixel-wide lines in the ABF image. Evaluation was performed with Gatan *DigitalMicrograp*h.

Figure 1

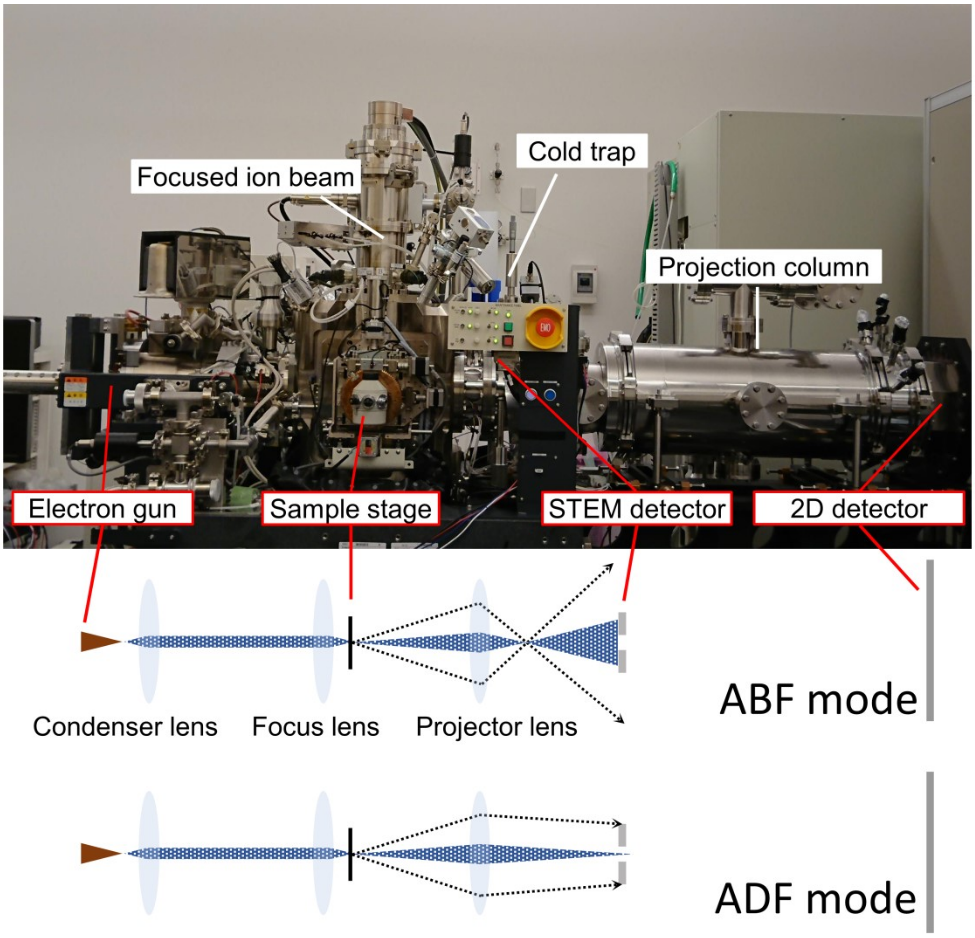

Figure 2

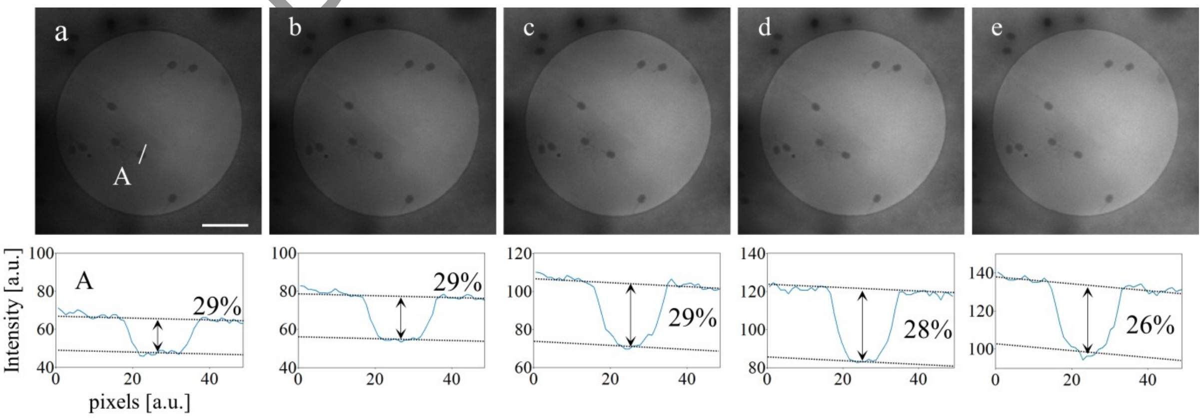

Figure 3

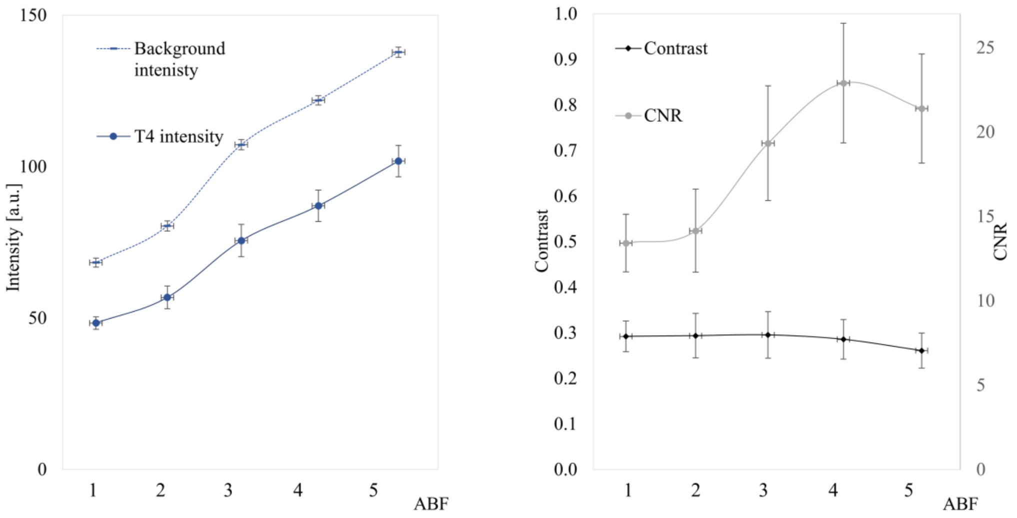

Figure 4

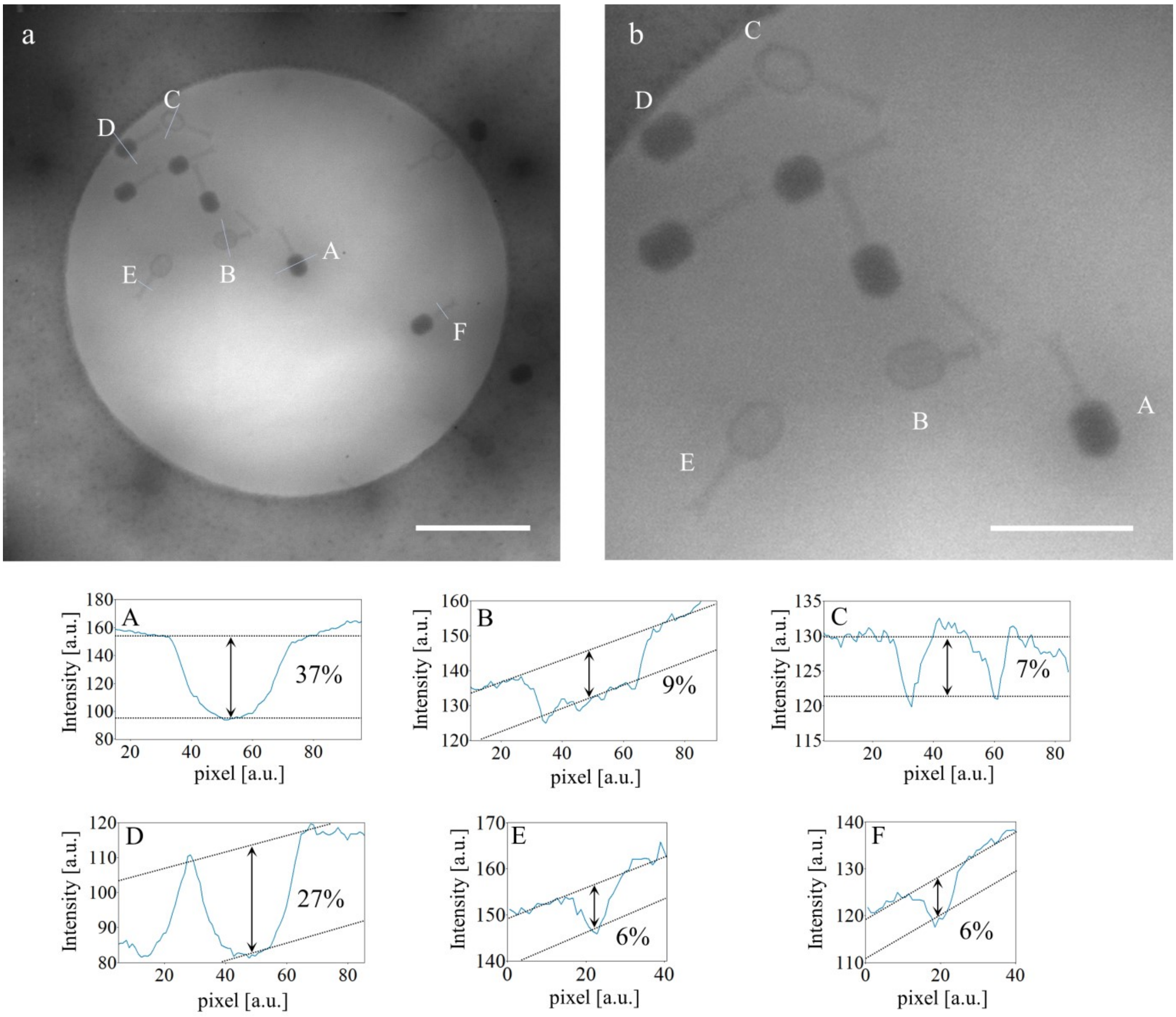

Figure 5

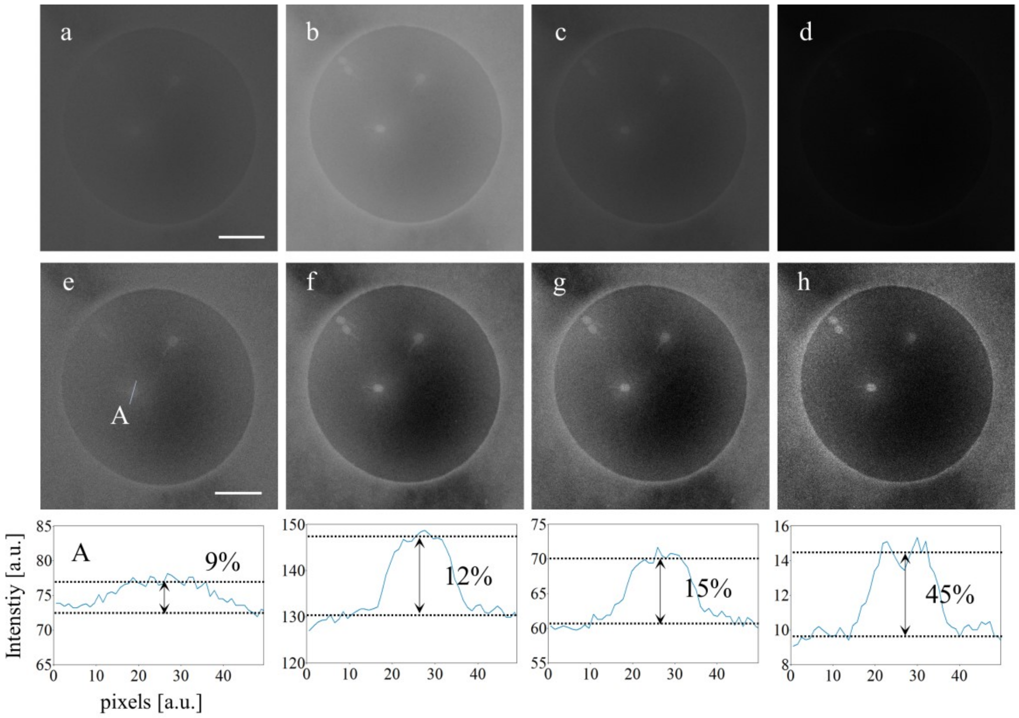

Figure 6

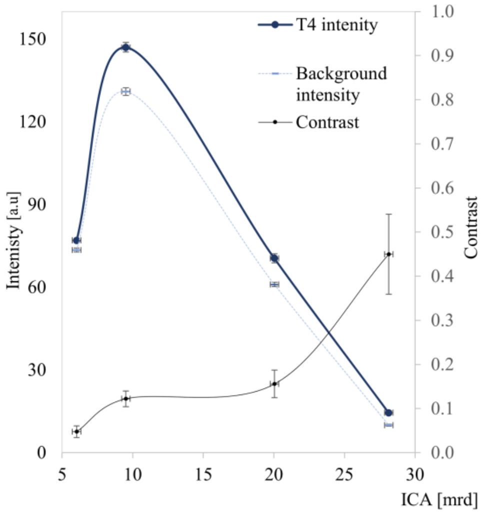

Figure 7

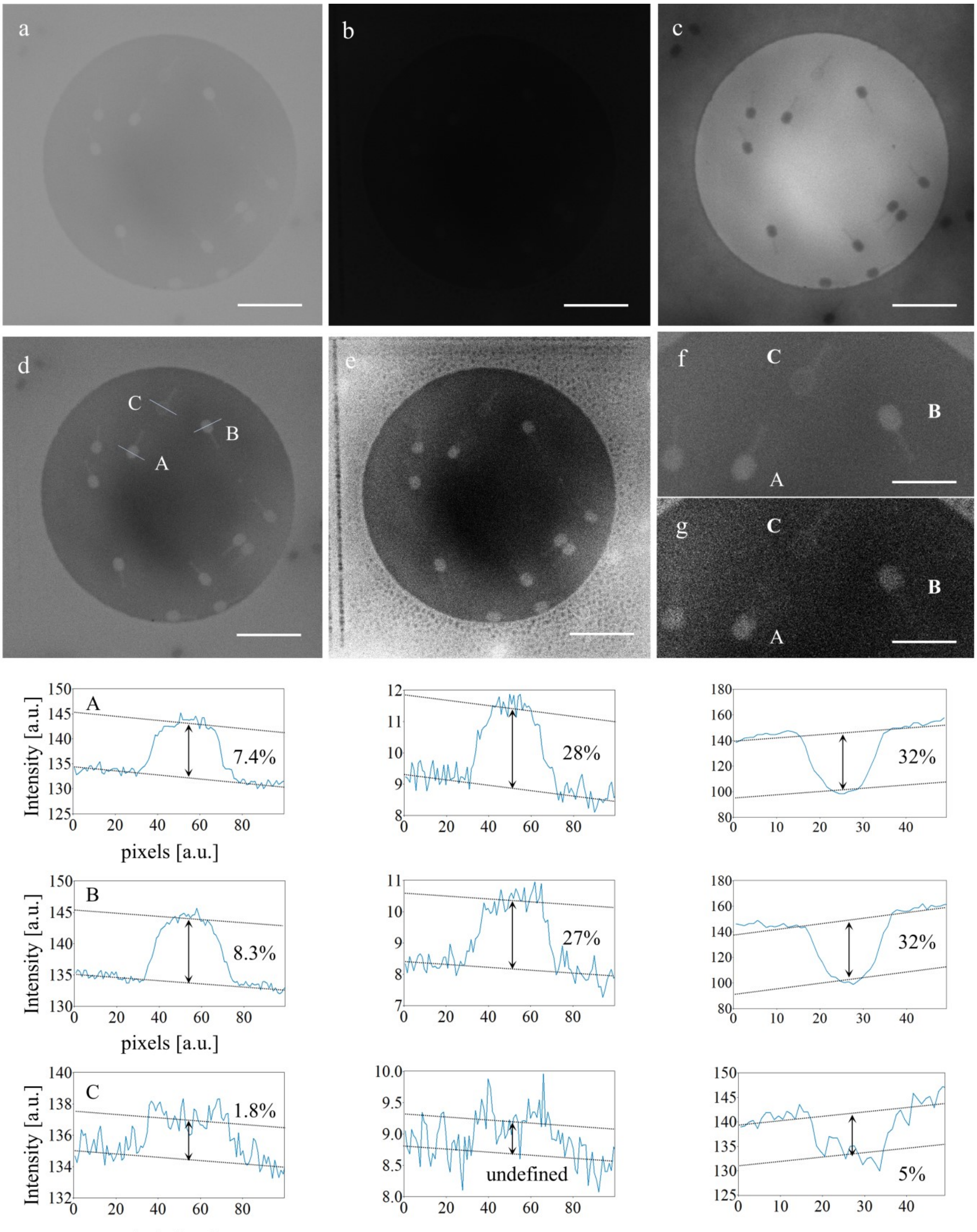
a
b
c
d
C
B
A
e
f
C
B
A
g
C
B
A
A
7.4%
28%
32%
B
8.3%
27%
32%
C
1.8%
undefined
5%
Intensity [a.u.]
pixels [a.u.]
150
145
140
135
130
125
0
20
40
60
80
12
11
10
9
8
180
160
140
120
100
80
10
30
11
7
138
136
134
132
10.0
9.5
9.0
8.5
8.0